Available online at www.sciencedirect.com
ScienceDirect
Remote Sensing of Environment 111 (2007) 182 – 194
Remote Sensing of Environment
www.elsevier.com/locate/rse

Combined airborne laser and radar altimeter measurements over the Fram Strait in May 2002

K.A. Giles [a,*], S.W. Laxon [a], D.J. Wingham [a], D.W. Wallis [a], W.B. Krabill [b], C.J. Leuschen [c], D. McAdoo [d], S.S. Manizade [e], R.K. Raney [c]

[a] Centre for Polar Observation and Modelling, University College London, Gower Street, London, WC1E 6BT, UK
[b] NASA Goddard Space Flight Centre, Cryospheric Sciences Branch, Code 614.1, Wallops Island, VA 23337, USA
[c] Johns Hopkins University, Applied Physics Laboratory, 11100 Johns Hopkins Road, Laurel, MD 20723-6099, USA
[d] NOAA, E/RA31, SSMC1, Room 5402, Laboratory for Satellite Altimetry, 1335 East-West Highway, Silver Spring, Maryland 20910-3282, USA
[e] EG&G Technical Services, NASA Wallops Flight Facility, Building N-159, Wallops Island, VA 23337, USA

Received 1 August 2006; received in revised form 1 February 2007; accepted 10 February 2007

Abstract

Knowledge of sea ice thickness is critical for the prediction of future climate, and for assessing the significance of changes in thickness. Sea ice thickness can be calculated from radar or laser satellite altimetry measurements of freeboard. However, a lack of knowledge of snow depth introduces significant uncertainties into these calculations.

This paper compares the first coincident airborne laser and radar altimetry data over sea ice, collected during the Laser Radar Altimetry (LaRA) field campaign. LaRA was a flight of opportunity that provided valuable data to explore techniques to validate satellite measurements of ice freeboard, and the possibility of combining laser and radar measurements over snow covered sea ice to calculate the snow depth. Two new methods were created to analyse these data sets: a new radar retracker and a radar power simulator, which models radar returns from the laser data.

We present the first quantitative analysis of data from the LaRA laser and radar altimeters, and demonstrate the potential of combining laser and radar altimetry to estimate snow depth. LaRA elevation estimates compare well with elevations from the radar altimeter onboard ERS-2 at the sub-meter level and the study provides lessons for future validation of satellite altimetry data over sea ice. Laser elevations are consistently higher than the radar elevations over snow covered sea ice. As LaRA was a flight of opportunity, no coincident in-situ measurements were available. Nevertheless, the difference between the reflecting surface of the laser and radar is consistent with snow depth from climatology and the analysis techniques developed in this paper will be useful for future radar and laser altimetry comparisons.

Keywords: Radar altimetry; Laser altimetry; Sea ice thickness; Snow depth

1. Introduction

Knowledge of Arctic sea ice thickness is critical to our estimates of sea ice reduction and consequently increased fresh water input into the Greenland, Iceland and Norwegian Seas, a factor that may ultimately affect the thermohaline circulation (Aagaard & Carmack, 1989). Sea ice also inhibits the transfer of heat, moisture and momentum between the atmosphere and the ocean (Ledley, 1993) and has a high albedo compared to the ocean (Curry et al., 1995), so is an important component in climate models. Therefore, systematic, basin-wide estimates of sea ice thickness are required for both model improvement (Rothrock et al., 2003) and trend detection (McLaren et al., 1990). While analyses of passive microwave satellite data have provided a record of sea ice extent for approximately the past 30 years (Comiso, 2006), in-situ ice thickness measurements are spatially and temporally limited (Bitz et al., 2001). One of the two main objectives of the forthcoming European Space Agency satellite radar altimetry mission, CryoSat-2, is to provide an estimate of the trend in spatially averaged sea ice thickness (Wingham et al., 2001).

* Corresponding author.
E-mail address: k.giles@cpom.ucl.ac.uk (K.A. Giles).

0034-4257/$ - see front matter © 2007 Elsevier Inc. All rights reserved.
doi:10.1016/j.rse.2007.02.037

Table 1
Typical values of parameters in Eqs. (3) and (4), the error in the calculation of sea ice thickness for radar and laser altimetry respectively, for May

Parameter	Typical value	Reference	Error estimate	Reference
Ice freeboard [1] (f_i)	0.3 m	Haas (2002)	0.03 m	Giles and Hvidegaard (2006)
Snow freeboard (f_s)	0.6 m	From f_i and h_s	0.02 m	Kwok et al. (2004)
Snow depth (h_s)	0.3 m	Warren et al. (1999)	0.11 m	Warren et al. (1999), RMS on h_s for May
Water density (ρ_w)	1023.8 kg m^{-3}	Wadhams et al. (1992)	0.5 kg m^{-3}	Wadhams et al. (1992)
Ice density (ρ_i)	915.1 kg m^{-3}	Wadhams et al. (1992)	5 kg m^{-3}	Wadhams et al. (1992)
Snow density (ρ_s)	319.5 kg m^{-3}	Warren et al. (1999)	3 kg m^{-3}	Warren et al. (1999)

[1] Assumes that at least 50 individual freeboard estimates are summed in-order to estimate the mean ice freeboard.

Measurements of sea ice freeboard from satellites (carrying either radar or laser altimeters) have been used to calculate sea ice thickness on a basin wide scale (Laxon et al., 2003) and on a local scale (Kwok et al., 2004). Sea ice thickness is calculated by measuring the elevation of the ice above the water (ice freeboard) if using a radar altimeter, or ice plus snow (snow freeboard) if using a laser altimeter, and assuming hydrostatic equilibrium. The equations to calculate sea ice thickness from freeboard measurements by radar and laser altimeters respectively are

$$h_i = \frac{f_i \rho_w}{(\rho_w - \rho_i)} + \frac{h_s \rho_s}{(\rho_w - \rho_i)} \tag{1}$$

$$h_i = \frac{f_s \rho_w}{(\rho_w - \rho_i)} + \frac{h_s(\rho_s - \rho_w)}{(\rho_w - \rho_i)} \tag{2}$$

where f_i is the radar measured ice freeboard and f_s is the laser measured snow freeboard, h_i, ρ_i and h_s, ρ_s are the thicknesses and densities of the ice and snow respectively and ρ_w is the density of the water.

However, there are uncertainties associated with both these techniques. If we are to use these data sets with confidence we must understand the errors associated with calculating ice thickness, and reduce these errors to a level useful for trend detection and model validation.

The main error sources are:

For radar altimetry;

1) Uncertainty in the location of the radar scattering surface in the snow/ice system. Laxon et al. (2003) assume that the radar reflects from the snow/ice interface. This assumption is based on laboratory measurements by Beaven et al. (1995). However, there are no direct observations to confirm this assumption.

For both radar and laser altimetry;

2) The snow loading/height uncertainty. Both Laxon et al. (2003) and Kwok et al. (2004) estimate snow depth from snow climatology (Warren et al., 1999). Assuming that the uncertainties are uncorrelated, the errors (to the first order) in ice thickness calculated from radar (ε_r^2) and laser (ε_l^2) altimeter estimates of ice/snow freeboard are

$$\begin{aligned}\varepsilon_r^2 = {} & \varepsilon_{fi}^2\left(\frac{\rho_w}{(\rho_w-\rho_i)}\right)^2 + \varepsilon_{hs}^2\left(\frac{\rho_s}{(\rho_w-\rho_i)}\right)^2 + \varepsilon_{\rho s}^2\left(\frac{h_s}{(\rho_w-\rho_i)}\right)^2 \\ & + \varepsilon_{\rho w}^2\left(\frac{f_i}{(\rho_w-\rho_i)} - \frac{f_i\rho_w}{(\rho_w-\rho_i)^2} - \frac{h_s\rho_s}{(\rho_w-\rho_i)^2}\right)^2 \\ & + \varepsilon_{\rho i}^2\left(\frac{f_i\rho_w}{(\rho_w-\rho_i)^2} + \frac{h_s\rho_s}{(\rho_w-\rho_i)^2}\right)^2\end{aligned} \tag{3}$$

$$\begin{aligned}\varepsilon_l^2 = {} & \varepsilon_{fs}^2\left(\frac{\rho_w}{(\rho_w-\rho_i)}\right)^2 + \varepsilon_{hs}^2\left(\frac{\rho_s}{(\rho_w-\rho_i)} - \frac{\rho_w}{(\rho_w-\rho_i)}\right)^2 \\ & + \varepsilon_{\rho s}^2\left(\frac{h_s}{(\rho_w-\rho_i)}\right)^2 + \varepsilon_{\rho w}^2\left(\frac{f_s}{(\rho_w-\rho_i)} - \frac{h_s}{(\rho_w-\rho_i)}\right. \\ & \left. - \frac{f_s\rho_w}{(\rho_w-\rho_i)^2} - \frac{h_s\rho_s}{(\rho_w-\rho_i)^2} + \frac{h_s\rho_w}{(\rho_w-\rho_i)^2}\right)^2 \\ & + \varepsilon_{\rho i}^2\left(\frac{f_s\rho_w}{(\rho_w-\rho_i)^2} + \frac{h_s\rho_s}{(\rho_w-\rho_i)^2} - \frac{h_s\rho_w}{(\rho_w-\rho_i)^2}\right)^2\end{aligned} \tag{4}$$

where $\varepsilon_{\rho i}$, $\varepsilon_{\rho w}$, $\varepsilon_{\rho s}$ are the uncertainties in the density of ice, water and snow, ε_{hs} is the uncertainty in the snow height and ε_{fi} and ε_{fs} are the uncertainties in the radar measured freeboard and laser measured freeboard, respectively.

Substituting the values in Table 1 into Eqs. (3) and (4) gives

$$\begin{aligned}\varepsilon_r^2 &= \varepsilon_{fi}^2 88.56 + \varepsilon_{hs}^2 8.62 + \varepsilon_{\rho s}^2 8\times10^{-6} + \varepsilon_{\rho w}^2 9.79\times10^{-4} \\ &\quad + \varepsilon_{\rho i}^2 1.16\times10^{-3} \\ \varepsilon_r^2 &= 0.08 + 0.10 + 6.8\times10^{-5} + 2.5\times10^{-4} + 2.9\times10^{-2} \\ \varepsilon_r &= 0.46m\end{aligned} \tag{5}$$

$$\begin{aligned}\varepsilon_l^2 &= \varepsilon_{fs}^2 88.56 + \varepsilon_{hs}^2 41.92 + \varepsilon_{\rho s}^2 8\times10^{-6} + \varepsilon_{\rho w}^2 9.8\times10^{-4} \\ &\quad + \varepsilon_{\rho i}^2 1.6\times10^{-3} \\ \varepsilon_l^2 &= 0.04 + 0.51 + 6.8\times10^{-5} + 2.5\times10^{-4} + 2.9\times10^{-2} \\ \varepsilon_l &= 0.76m.\end{aligned} \tag{6}$$

The largest contribution to the error in ice thickness is due to the uncertainty in snow depth (h_s), and the error due to the uncertainty in snow depth is a factor of two greater for the laser case than the radar case.

The Laser Radar Altimetry (LaRA) field campaign was conducted as part of a National Oceanic and Atmospheric Administration (NOAA)/National Aeronautics and Space Administration (NASA)/European Space Agency (ESA) collaboration. LaRA was a flight of opportunity over sea ice between Svalbard and Greenland, which took place during a campaign to measure land ice.

LaRA was the first airborne field campaign to carry both a laser and a CryoSat (Wingham et al., 2006) type radar altimeter. It was designed to under-fly the ESA satellites Envisat and ERS-

2, which carry radar altimeters. Although the satellite data were limited (Envisat suffered technical problems), LaRA provided the opportunity to explore techniques to validate satellite measurements of sea ice freeboard, and to explore whether radar and laser measurements over sea ice can be combined to estimate snow height. Two methods were used to analyse the data. Firstly a new retracker was designed to estimate the absolute elevation from the radar echoes. Secondly we estimated the difference between laser and radar elevations by simulating the radar return from a surface constructed from the laser data (the D2P (Delay/Doppler Phase-monopulse Radar Altimeter) power simulator). After simulating an echo from the laser data we calculated the offset in the range window between the simulated and D2P measured echoes using a cross-correlation technique. We then used this offset to calculate the difference in elevation between the laser and radar-measured surfaces. The use of this new technique means that we have calculated the difference in elevation between the laser and radar measured surface as if each surface had been measured by the same instrument, rather than comparing data from two instruments that sampled the surfaces in different ways. In this paper we present the first quantitative comparison of coincident laser and radar altimetry over sea ice and describe two new methods to analyse such data.

2. The LaRA experiment

2.1. The location of the LaRA field campaign

The LaRA flights took place on the 20th and 23rd May 2002 from Svalbard. Fig. 1 shows the flight paths, which were designed to under-fly Envisat/ERS-2 over-passes to within a few hours. However, only data from ERS-2 was available due to a fault with Envisat. On the 20th May, take-off was at 09.28 GMT and the last sea ice data were collected at 14.20, ERS-2 over-flew the LaRA flight path at 15.50. On the 23rd May, take-off was at 12.00, and the aircraft arrived back in Svalbard at 18.00, ERS-2 over-flew at 15.55. The daily maximum 2 m air temperatures, from the European Centre for Medium-Range Weather Forecasts (ECMWF) operational data, show that the temperature remained below 0 °C over the survey region during both days (ECMWF, 2002). Calibration flights took place over the runway at the Wallops Flight Facility on the 3rd May 2002. The Radar and laser elevation estimates were calibrated against elevation estimates from a survey of the runway by a GPS antenna mounted on a truck.

2.2. The LaRA payload

LaRA flights took place onboard the NASA P-3 aircraft, which carried: the John Hopkins University, Applied Physics Laboratory (JHU/APL) D2P Ku Band (13.9 GHz) Radar Altimeter (Raney, 1998); two NASA laser altimeters, with a wavelength equal to 532 nm, called the Airborne Topographic Mappers (ATM) (Csathó et al., 1996); and two digital cameras mounted on the fuselage, taking images of the ice below. The P-3 was also equipped with a Global Positioning System (GPS) receiver and an Inertial Navigation System (INS). Fig. 2 shows the layout of the

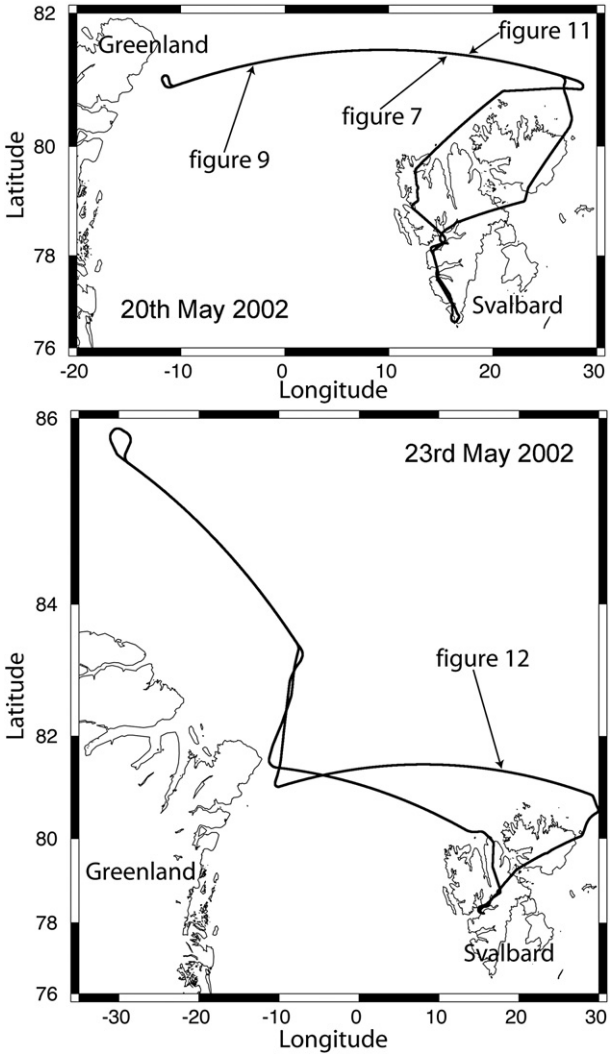

Fig. 1. Locations of the LaRA flight lines for the 20th and 23rd May 2002. The locations of the data shown in Figs. 7,9,11 and 12 are also shown.

instruments and Fig. 3 shows the footprint geometry for the D2P, ATMs and the digital camera for an altitude of 500 m.

2.3. Initial data processing

The ATM data and digital photographs were processed by NASA at the Wallops Flight Facility to produce geo-located laser elevation estimates and images of the ice (Krabill et al., 2002). The raw D2P data were processed at APL along with the geo-location data from the Wallops Flight Facility using the delay-Doppler algorithm (Raney, 1998) to produce geo-located radar waveforms. The delay-Doppler process focuses the radar footprint in the along track direction to produce the rectangular footprints shown in Fig. 3. Initial results from APL are described in Leuschen and Raney (2005).

2.4. Data processing

The D2P records the returned power in a range window, which is 512, 256, 128 or 64 bins wide, depending on the transmitted pulse length (Raney & Leuschen, 2003). The on-

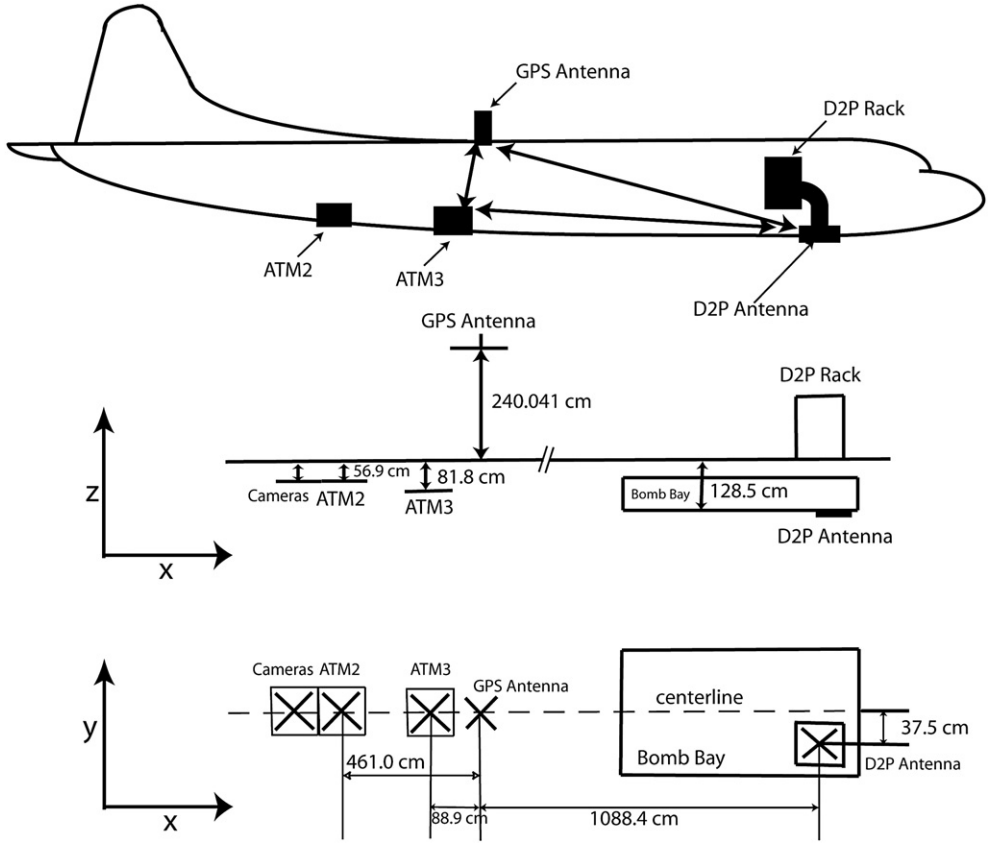

Fig. 2. Sensor layout in the P-3 aircraft, adapted from Raney and Leuschen (2003). The D2P is the radar altimeter and the ATMs are laser altimeters. *X* is the flight direction, *Y* is in the direction of the port wing and *Z* is the vertical axis.

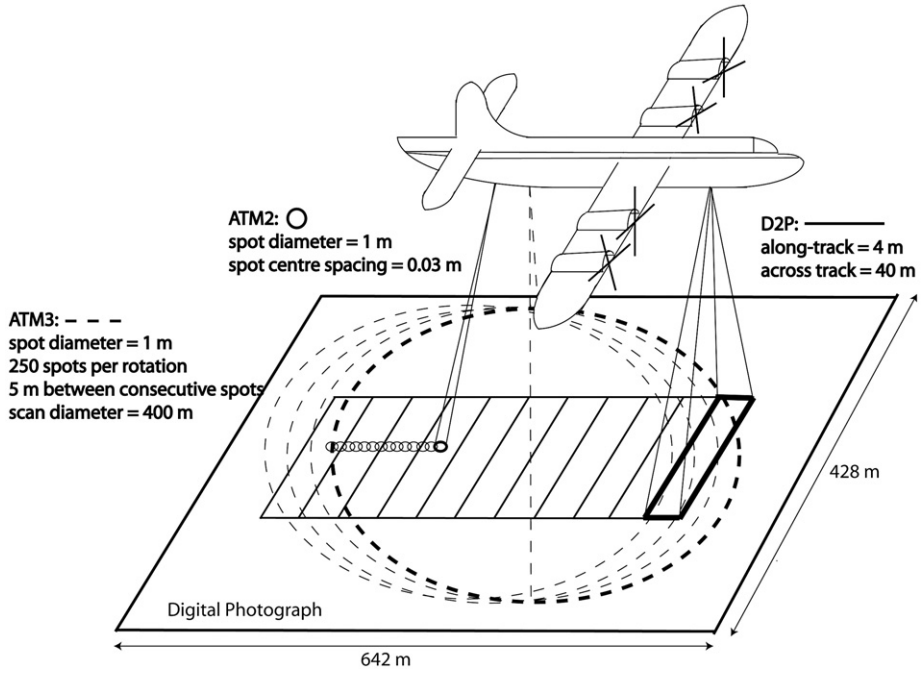

Fig. 3. LaRA footprint geometry for the P-3 at an altitude of 500 m and velocity of 150 ms^{-1}. The D2P is the radar altimeter and the ATMs are laser altimeters. ATM2 operated in profiling mode while ATM3 operated in scanning mode. N.B. Figure is not drawn to scale.

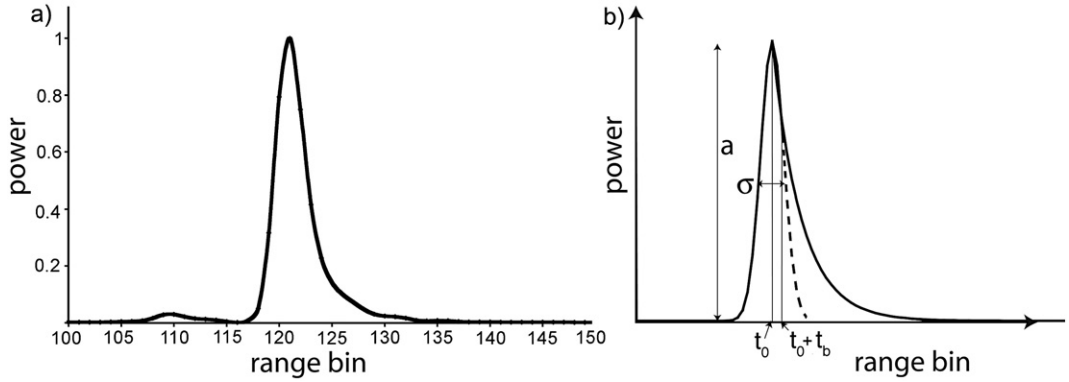

Fig. 4. a) Is a typical echo over a smooth surface. The small rise at bin 110 appears in all data and is a sidelobe of the radar. One bin corresponds to 0.208 m in range. b) Shows the model echo and retracking function parameters (Eq. (7)).

board tracking computer attempts to keep the surface reflection point in the centre of the range window during the flight for all range window lengths apart from 512, which is tracked 1/4 of the way from the beginning of range window. Retracking is a post-flight method of obtaining a more accurate elevation estimate from the recorded D2P waveform (Ferraro & Swift, 1995).

We employed two processing techniques: Firstly we designed a new retracking algorithm to enable us to make an elevation estimate from the radar data; Secondly we designed the D2P power simulator, a new alternative to a conventional retracking algorithm, which calculates D2P type echoes from the laser data. We then used the simulated and D2P measured echoes to calculate the difference in elevation between the laser and radar-measured surfaces. This second processing technique was created as the analysis of the echoes showed a highly variable echo shape, which degraded the accuracy of the elevation estimate obtained when using a conventional re-tracker.

2.4.1. The D2P retracking algorithm

We designed a new retracker based on the same method as Wingham et al. (2006). Our retracking algorithm was an empirically derived function designed to work with echoes conforming to the shape of echoes over a flat surface, hereafter referred to as typical echoes. Fig. 4 shows an example of a typical echo.

We used two functions to describe the shape of a typical echo: the first part of the echo was represented by a Gaussian (where $f=f_1$ in Eq. (7)) and the second part by an exponentially decaying function (where $f=f_2$). These two functions were linked by a third function (where $f=f_L$). The full retracking function is

$$P_r(t;a,t_0,k,\sigma) = ae^{-f(t)^2} \tag{7}$$

where

$$f(t) = f_1(t) = \frac{(t-t_0)}{\sigma} \qquad -\infty<t<t_0$$

$$f(t) = f_l(t) = a_3(t-t_0)^3 + a_2(t-t_0)^2 + \frac{1}{\sigma}(t-t_0) \qquad t_0<t<(t_b+t_0)$$

$$f(t) = f_2(t) = (k(t-t_0))^{1/2} \qquad (t_b+t_0)<t<\infty$$

where $P_r(t)$ is the power at time t, a is the maximum amplitude of the echo, t_0 is the time that $P_r=a$, t_b is the time period for which $f=f_L$, σ is the standard deviation of the Gaussian function and k governs the rate of decay of the exponentially decaying function. a_2 and a_3 are chosen such that the function P_r, and it's first derivative, are smooth and continuous.

The retracking algorithm minimises the chi-squared value of a least squares fit between the waveform data points and the non-linear function (Eq. (7)) by varying a, σ, t_0 and k. We took t_0 as the time delay to the surface and calculated the difference between t_0 and the centre (or 1/4 point for the 512 length waveform) of the range window to compute the retracking correction. The correction was then added to the elevation estimate from the tracking computer.

To estimate the bias of our retracker we used the calibration data set and averaged the GPS truck survey elevation estimates over the D2P footprint, weighting them with the D2P antenna pattern (see Appendix Eq. (12)). The GPS elevation estimates were consistently higher than the D2P elevation estimates by, on average, 0.034 m. Therefore we added 0.034 m to all D2P elevation estimates. To cross-calibrate the D2P and ATM3, ATM3 elevation estimates were averaged over each D2P footprint, as for the D2P calibration. The mean difference between the D2P and ATM3 elevation estimates was very low at −0.0017 m (the difference was averaged over 60 measurements). However, at single comparison points, the difference between the radar and laser elevation estimates was up to 0.05 m.

To compare the D2P and ATM3 data over sea ice the ATM3 elevations were averaged over each D2P footprint as described above. Measurements from both the fore and aft parts of the laser scan were included in each average in order to minimise errors caused by drifts in the INS. To compare the elevation estimates from LaRA and ERS-2, we calculated a running mean over 2 km (the approximate size of the ERS-2 altimeter footprint) for both data sets.

2.4.2. The D2P power simulator

Although the re-tracker provided elevations estimates for comparison to ERS elevation estimates (Section 3), detailed inspection of the performance of the re-tracker over individual echoes revealed that the echo shape was highly variable, which

degraded the accuracy of the elevation estimate. As the origin of the non-typical echoes was not clear we designed a radar simulator to investigate whether we could re-create non-typical echoes and to provide an improved method for estimating the difference in elevation between the surfaces measured by the radar and laser altimeters. We designed the D2P power simulator to calculate a D2P radar echo using a surface model constructed from the ATM3 laser data. The surface model was constructed by using a Gaussian function (where $\sigma = 4$ m) to smooth the laser elevation estimates, from both the fore and aft parts of the scan, to points positioned at four meter intervals. It was then divided into triangular facets to create area elements.

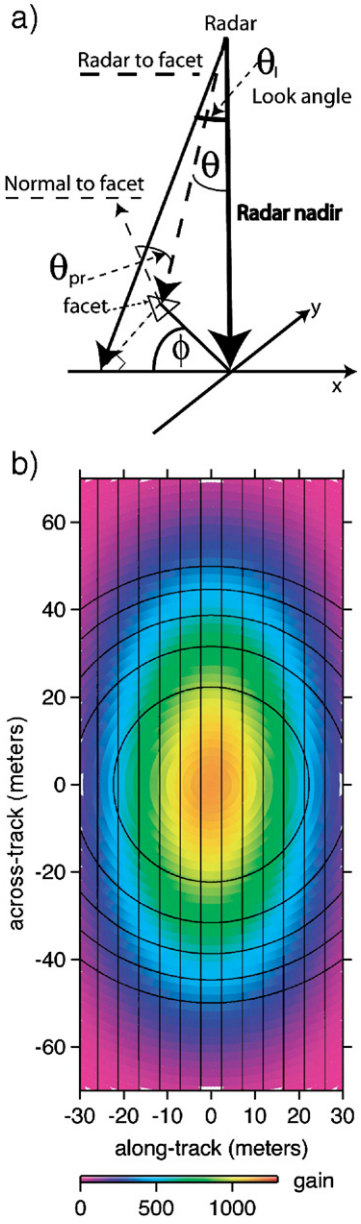

Fig. 5. a) The facet orientation angles, the look angle and the angle between the vector normal to the facet and the vector from the radar to the facet. Axes as in Fig. 2. b) Components of the power integral. The graded coloured area shows the variation of the antenna gain $G(\theta,\phi)$ (linear scale). The vertical lines show the width of the along-track footprint, due the along-track processing, $\beta(\theta_l)$. The circles show the transmitted power envelope $P(t)$ intersecting the surface. The first circle shows the area of the pulse limited footprint (Mantripp, 1996), subsequent circles are multiples of this area (range rings). The radar nadir is located at (0,0).

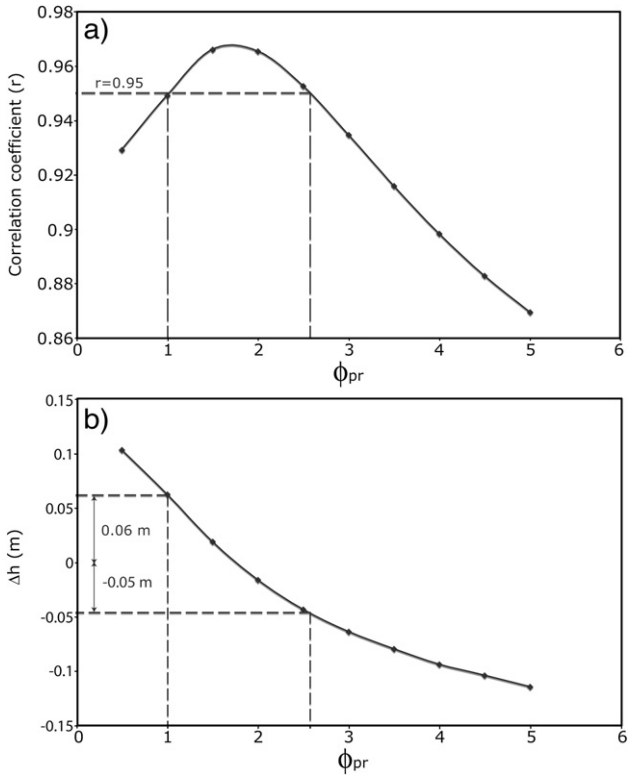

Fig. 6. Uncertainty in Δh due to variability in the polar response angle. a) Shows the correlation coefficient as a function of ϕ_{pr}. $r > 0.95$ between $\phi_{pr} = 1.01°$ and $\phi_{pr} = 2.58°$. $\phi_{pr} = 1.75°$ provides the best fit to the calibration data as the echoes over the runway were typically narrower than those over sea ice. b) Shows Δh as a function of ϕ_{pr}. Δh has a range of ± 0.06 m when $r > 0.95$.

The power integral that forms the bases of the simulator is

$$\int_A \int \frac{P(t)}{r^4} G^2(\theta,\phi)\beta(\theta_l)P_{res}(\theta_{pr},\phi_{pr})\mathrm{d}A \quad (8)$$

where A is area and r is the range to the surface. $P(t)$, describes the power envelope as a function of time; $G(\theta,\phi)$, describes the antenna gain as a function of the area element orientation angles, $\beta(\theta_l)$, describes the weighting from the along track synthetic aperture processing as a function of look angle and $P_{res}(\theta_{pr},\phi_{pr})$ approximates the polar response of the facet as a function of the angle between the vector normal to the facet and the vector between the D2P antenna and the facet (θ_{pr}) and the polar response angle (ϕ_{pr}), which represents the fall off in power as a function of incidence angle (Fetterer et al., 1992). We chose $\phi_{pr} = 5°$ for our simulator as this angle allowed the simulator to create both typical and non-typical echoes and is consistent with measurements of ϕ_{pr} from aircraft (Parashar et al., 1974). $P(t)$, $G(\theta,\phi)$, $\beta(\theta_l)$ and $P_{res}(\theta_{pr},\phi_{pr})$ are described in detail the Appendix. The aircraft attitude parameters of pitch and roll[1]

[1] Variations in the yaw of the aircraft were found to have little affect on the echo shape.

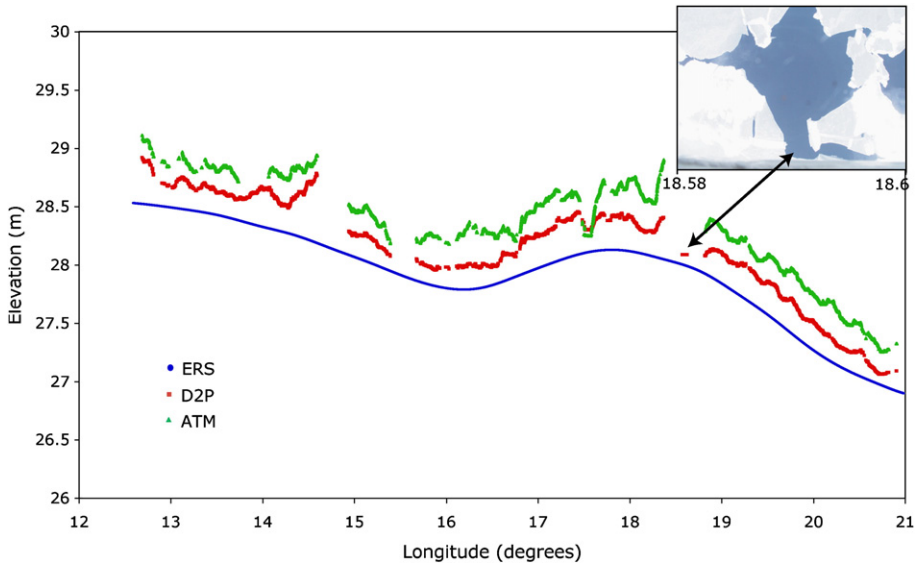

Fig. 7. ATM elevation (green) averaged over the D2P footprint and weighted by the antenna pattern, D2P elevation (red) re-tracked using the function described by Eq. (7) and ERS-2 mean sea surface (blue). Elevations are with respect to the World Geodetic System (WGS-84) reference ellipsoid and have been smoothed by calculating a running mean over two km. Data gaps occur where there is insufficient data for averaging due to; for the laser case, a lack of returns over open water or anomalously high elevations measurements due to cloud cover, and for the radar case, where the GPS data were not available and/or the radar was not tracking. The photograph is the coincident digital imagery for the section of track indicated by the arrow (18.58° to 18.6° longitude).

were also included in the simulator as variations in these parameters affect the shape of the radar return. The integral was evaluated numerically.

The look angle, orientation angles and θ_{pr} are shown in Fig. 5a. Fig. 5b shows how components of the power integral, $P(t)$, $G(\theta,\phi)$ and $\beta(\theta_l)$, combine.

To determine the difference between the simulated and D2P measured waveforms we calculated the correlation coefficient (r) between the waveforms for different shifts of the position of the D2P measured waveform in the range window. The shift that resulted in the maximum correlation coefficient, measured in bins and fractions of bins, was then converted to an offset (Δh), measured in meters, i.e. Δh is the difference in elevation between the laser and radar-measured surfaces, laser minus radar. We only use echoes where r is greater than 0.95 (25% of the echoes were discarded). The calibration flights over the Wallops runway were used to calibrate the D2P power simulator. Over the runway we expect that Δh will be zero as the radar and the laser will reflect from the same surface. We found a bias in Δh of −0.087 m. Therefore, we have added 0.087 m to all values of

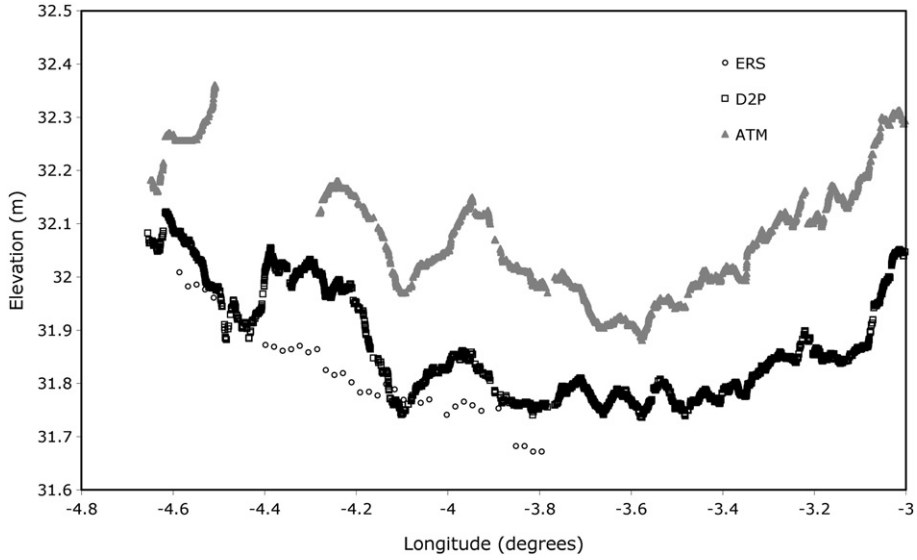

Fig. 8. ATM elevation (grey triangles) averaged over the D2P footprint and weighted by the antenna pattern, D2P elevation (black squares) re-tracked using the function described by Eq. (7) and ERS-2 ice surface elevation (black circles). The data has been smoothed by calculating a running mean over two km. Elevations are with respect to the WGS-84 reference ellipsoid. Data gaps occur in the laser data due to a lack of returns over open water or anomalously high elevations measurements due to cloud cover.

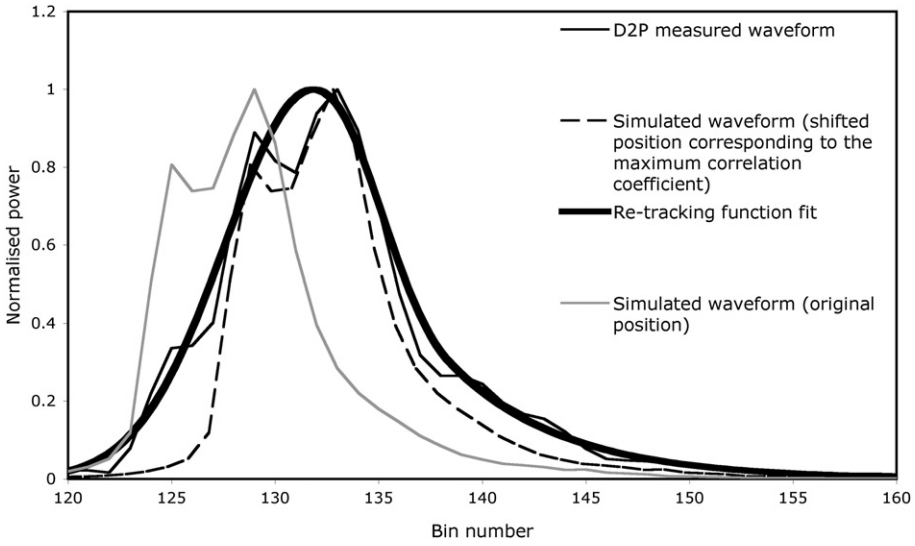

Fig. 9. An example of a D2P measured, non-typical echo (thin black line) with the retracking function fit to the waveform (thick black line) and the simulated waveform (grey/dashed). The figure shows the original position of the simulated waveform (grey) and the shifted position of the simulated waveforms (dashed), corresponding to the maximum correlation coefficient.

Δh. To estimate the error in Δh due to assuming a constant polar response angle (ϕ_{pr}), we first calculated the correlation coefficient for different values of ϕ_{pr} (Fig. 6a). As we only use values of Δh where r is greater than 0.95, we then calculated the difference in Δh between the maximum r value and the $r=0.95$ values (Fig. 6b). Therefore, from Fig. 6b, we estimate the uncertainty in Δh to be ± 0.06 m.

3. Coincident LaRA and ERS-2 measurements

The elevation estimates from LaRA data presented in this section were calculated using the retracking algorithm and method described in Section 2.4.1. Data gaps in the laser data are due to the removal of anomalously high elevation estimates resulting from returns from cloud cover, or the removal of anomalously low elevation estimates over open water where the return is from scattering within the water column. Data gaps may also occur over open water as all the energy can be totally forward-scattered into the water column, therefore no return signal is received at the altimeter. Data gaps in the radar data occur where the GPS data were not available and/or where the radar was not tracking, both radar and laser elevations are not calculated at these points. Fig. 7 shows a second section of track from the 20th May 2002. The blue line is the ERS-2 mean sea surface elevation, calculated from four years of ERS-2 data (Peacock & Laxon, 2004) and the red and green lines are the D2P and ATM elevations respectively.

The ERS-2 mean sea surface follows the elevation of the D2P and ATM data while remaining approximately 0.25 m below the D2P elevations. As ice freeboard typically ranges between 0.20 and 0.30 m we expect the ERS-2 mean sea surface to be below the D2P elevation estimates by this amount. By examining the digital photography between 18.58° and 18.6° longitude we find that the D2P was passing over open water and that the difference between the D2P elevation measurement and the ERS-2 mean sea surface is approximately nine cm. As the D2P is measuring the instantaneous (mean plus the time varying component) sea surface topography, while the ERS-2 profile represents a multi-year, mean sea surface, we would expect a difference between the two measurements.

The laser snow freeboard elevation estimates are higher than the radar ice freeboard and mean sea surface elevation estimates. The average difference between the laser and radar elevation estimates is 0.22 m, which is similar to values of snow depth from climatology (Warren et al., 1999). This is consistent with the assumption that the radar reflects from the snow/ice interface (Beaven et al., 1995) while the laser reflects from the air/snow interface (Kwok et al., 2004).

Fig. 8 shows a section of track from the LaRA return flight on the 20th May 2002. The LaRA elevation measurements (laser elevations shown by the grey triangles and radar elevations by the black squares) are plotted with ERS-2 estimates of

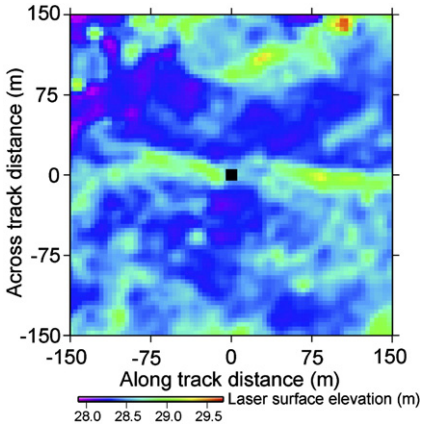

Fig. 10. Section of the laser surface model centered on the nadir location (black square) of the waveform shown in Fig. 9. Elevations are with respect to the WGS-84 reference ellipsoid.

ice elevation (black circles). Unfortunately, only a small number of ERS-2 returns were identified as originating from ice along this orbit (Peacock & Laxon, 2004). The centre lines of the ERS and LaRA ground tracks were separated by approximately 200 m. However ERS-2 overflew 154 minutes after the LaRA data were collected and, given typical drift speeds of 30 km per day in the Fram Strait, the ice may have moved up to 3 km between the aircraft and satellite overpasses.

ERS-2 carries a Ku band radar altimeter, therefore we would expect that spaceborne and airborne radars would measure the same surface. Fig. 8 shows the elevation estimates from ERS-2 and the D2P increasing as we move to the west and that elevation estimates from ERS-2 are closer to the elevation estimates from the D2P than to the laser elevation estimates. However, there are differences in the airborne and spaceborne radar elevation estimates that cannot be assigned to a single cause. They could be due to the fact that:

- The flights are not exactly coincident in space and time and therefore we may not be looking at the same ice.
- The footprints of the D2P and ERS-2 radar altimeter are different. The D2P's footprint is 40 m by 4 m where the diameter of the ERS-2 radar altimeter's pulse limited footprint is about 2 km. Therefore each instrument will sample the surface in a different way.
- The D2P retracker was designed for a typical echo shape (Fig. 4), however not all echoes conform to this shape (Fig. 9) which results in the accuracy of the elevation estimate from the D2P degrading as the shape of an echo moves away from that of a typical echo.

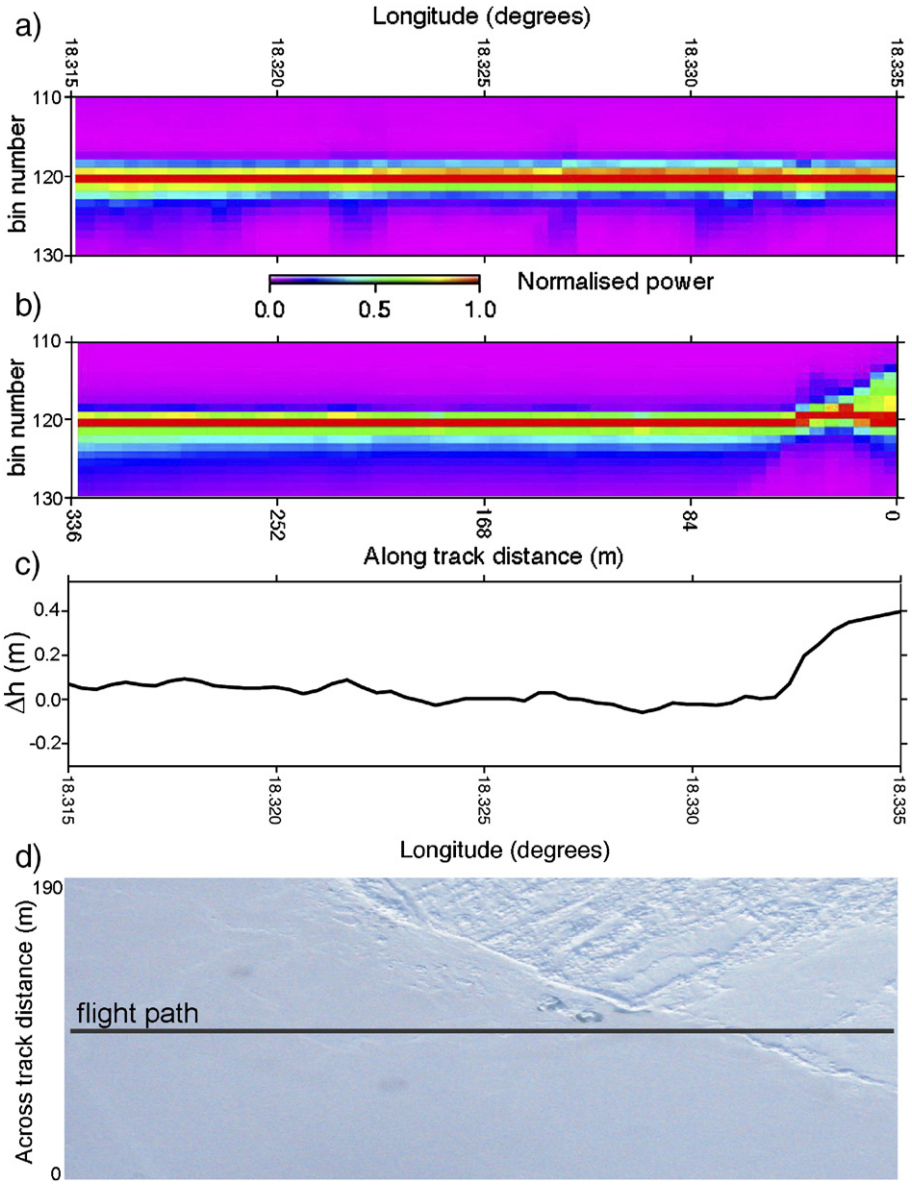

Fig. 11. a) D2P normalised power waveforms and b) simulator normalised power waveforms. The waveforms have been plotted vertically and the power in each bin assigned a colour according to its value, as shown by the scale bar. c) Δh (the data has not been smoothed). d) is the digital imagery of the ice over which the measurements were taken. The black line shows the flight path. The imagery has been stretched in the along track direction and cropped in the across track direction.

4. Results from the D2P power simulator

We now present the results from the D2P power simulator. As described in Section 2.4.2, the D2P simulator calculates a D2P waveform using a surface constructed from the laser data. This simulated waveform is then compared to the D2P measured waveform by calculating the correlation coefficient between the waveforms for different shifts of the position of the D2P measured waveform. The shift (in bins) at the maximum correlation coefficient is then converted to a difference in elevation (Δh) between the laser and radar measured surfaces, rather than providing an absolute elevation measurement.

4.1. Re-creating non-typical echo shapes

Fig. 9 shows a non-typical D2P measured waveform (thin black line), the retracking function fit (thick black line) and the simulated waveform (grey/dashed lines). The simulated waveform (grey line) arrives before the D2P measured waveform, therefore the laser is measuring a surface above the surface measured by the radar. The figure also shows the shifted position of the simulated waveform (dashed line), the shift corresponds to the position of the maximum correlation coefficient (0.98) between the D2P measured and simulated waveforms.

Fig. 10 shows the laser surface model for the area around the nadir location of the waveform in Fig. 9 (the ridge running across the figure in the along track direction is approximately 0.75 to 1 m above the surrounding surface). The two peaks in the waveform in Fig. 9 are separated by approximately 0.83 m, therefore it is likely that the waveform consists of a return from the ridge, followed by a return from the surrounding area.

The simulated waveform (dashed line) has been shifted by 3.8 bins, therefore $\Delta h = 0.88$ m. The re-track point of the retracking function falls between the two peaks and gives an elevation estimate of 27.34 m, the average laser elevation estimate over the D2P footprint is 28.69 m, therefore the difference

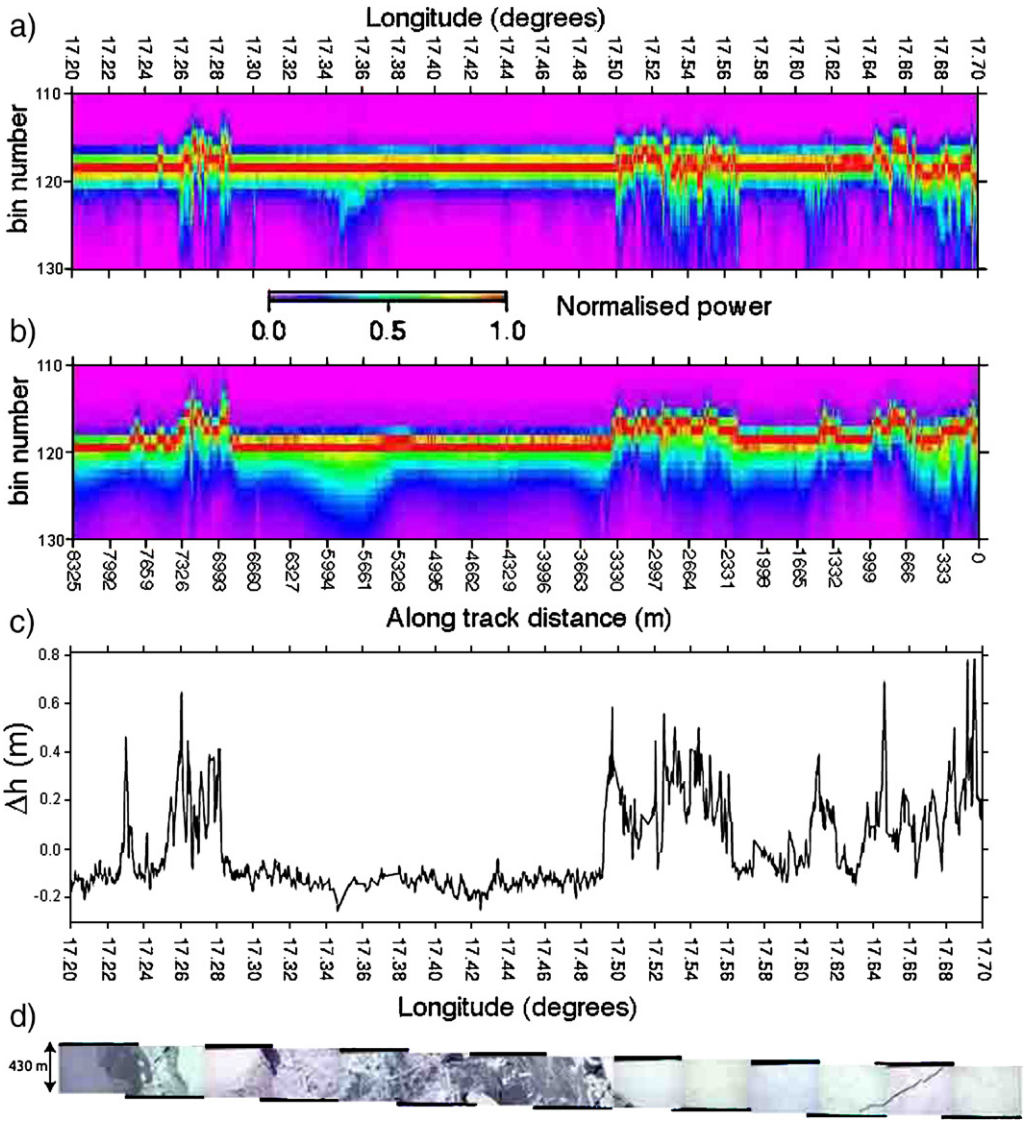

Fig. 12. a) D2P normalised power waveforms and b) simulator normalised power waveforms. c) Δh (the data has not been smoothed). d) is the digital imagery of the ice over which the measurements were taken.

between the laser and radar elevations, using method 1, is 1.35 m. These results show that the way a surface is sampled can affect the size of the laser–radar difference. For this case, there is a difference of 0.47 m between the retracker and the D2P power simulator.

4.2. Comparing coincident laser and radar measurements

Our first example shows data from the 20th May 2002. Fig. 11 shows a) the D2P measured data, b) the simulated data, c) Δh and d) digital imagery. In Fig. 11(b) we see a change on the right hand side of the simulated data from a smooth surface to a rougher surface. The change corresponds to the area in the photograph where the surface appears to become rougher. The D2P measured data Fig. 11(a) does not show this. The change in the simulated data is consistent with the depth of the snow increasing over this section (measured by the laser) and the radar continuing to measure the ice underneath. However, without in-situ snow depth measurements, it is not possible to confirm this.

Our second example, in Fig. 12, shows data from the 23rd May 2002. The digital photographs show thin, snow free, ice between 17.5° and 17.2° longitude. Across this section the position of the peak in both the waveform plots is constant, indicating a smooth surface. Over this thin, snow free, ice, we can assume that the laser and radar altimeters reflect from the same surface, therefore the negative values of Δh indicate a drift in the calibration since the calibration flights. While the ATMs were calibrated before and after every flight, calibration flights for the D2P were performed at the Wallops Flight Facility 17 days before the experiment and not repeated. The same bias (≈ -0.1 m) is apparent over other areas of thin, snow free ice.

4.3. Comparison of laser/radar difference with in-situ snow depth measurements

In-situ snow depth data were not collected during LaRA so we compare Δh to snow depth measurements from the Surface Heat Budget of the Arctic Ocean (SHEBA) site (Sturm et al., 2002) in Fig. 13. The SHEBA snow depths were collected during April and May 1998 in the Beaufort Sea. The snow depth climatology for May, from Warren et al. (1999) shows that the contours of snow depth in the Beaufort Sea and the at the top of the Fram Strait range between 0.28 m and 0.36 m, therefore we expect the distribution of snow depths in these two areas to be similar. Warren et al. (1999) also show that the mean snow depth across the whole Arctic reaches a maximum in May of 0.34 m, which compares well with the SHEBA mean snow depth and that the internal variability of the mean snow depth in May is 0.06 m, which is relatively small when compared to the mean values of snow depth. Therefore, in the absence of in situ-data, it is reasonable to compare the SHEBA snow depth data to Δh.

The average value of Δh is 0.2 m, if we take into account the likely calibration drift then the average value of Δh is 0.3 m. The probability distribution functions of Δh and the SHEBA snow depths both have a steep rise to the peak and a slower falloff at greater Δh/snow depths. The negative values of Δh in

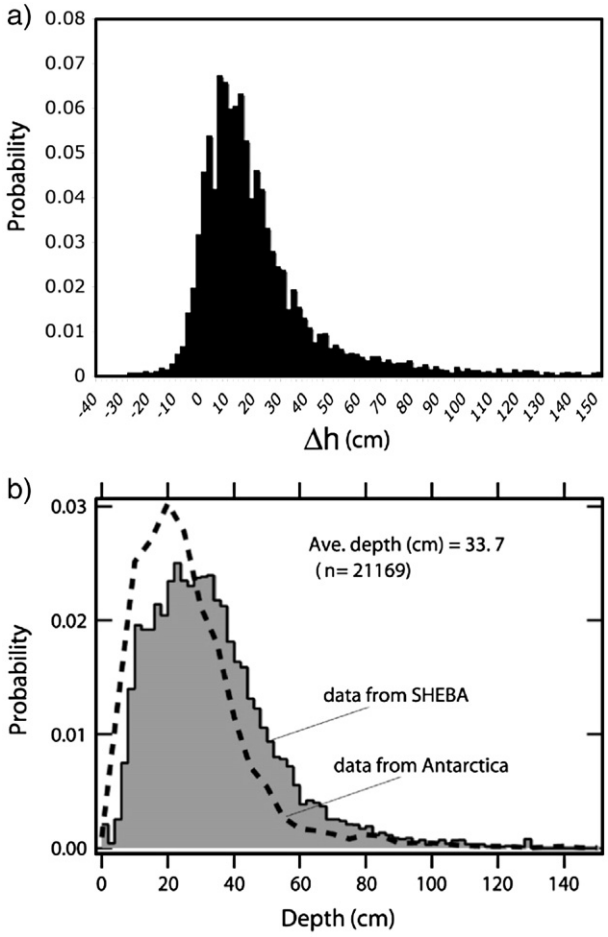

Fig. 13. a) The probability distribution function (PDF) for Δh for the western Fram Strait. The likely calibration drift of −0.1 m has not been corrected for, b) The PDF of snow depths during April and May 1998 near the SHEBA site (Sturm et al., 2002).

Fig. 13(a) are partly due to our error estimate of ±0.06 m and partly due to the likely calibration drift between the two instruments that occurred after the calibration flight.

5. Conclusions

We have analysed the first coincident airborne laser and radar altimetry data over sea ice, which, in addition, was also gathered beneath a satellite radar altimeter. The experiment was originally designed to validate spaceborne measurements of sea ice freeboard and to compare coincident laser and radar altimetry data elevations over snow covered sea ice. The results provide lessons for future validation of satellite altimetry data over sea ice and, for the first time, explore in a quantitative manner, the potential for combing laser and radar altimetry to estimate snow depth, the largest uncertainty in calculating sea ice thickness from altimeter measurements of ice/snow freeboard.

We used a newly developed retracker to retrieve ice and water elevations from the radar echo. Although this method allowed comparisons of the airborne and satellite elevation estimates at the sub-meter level, the uncertainties are too large to provide validation of the satellite ice thickness measurements to

the desired accuracy. Complex topography can, in some places, confuse the simple retracker and result in significant biases over rough ice surfaces. Our analysis also points to the need to ensure that airborne data is coincident in time and space with the satellite ground track to as high a degree as possible. Ideally the design of the survey area of the field campaign should also cover the extent of the satellite footprint or the area over which the satellite measurements are averaged. For radar altimeters, such as those onboard ERS-2 and Envisat, the survey area would need to be a few kilometers wide. By surveying the surface in this way one has the opportunity to sample the surface as the spaceborne instrument would have.

When comparing the laser and radar data on the aircraft we accounted for complex topography by designing a new algorithm (the D2P power simulator) to simulate the radar returns using the laser derived elevation data. The simulator accounts for varying surface topography as well as variations in the pitch and roll of the aircraft, which can also affect the shape of the radar's return echo. The results from the D2P power simulator demonstrated that the laser-measured surface was consistently higher than the radar-measured surface over snow covered sea ice, consistent with the hypothesis that the radar penetrates to the snow/ice interface. The difference in the elevation of the surface measured by the laser and radar altimeters (Δh) is typically 0.3 m (including the correction for the likely bias due to a drift in the calibration) and is consistent with observed snow depth. Moreover the distribution of Δh compares well to the snow depth distribution from Sturm et al. (2002). The results from this study show that elevation estimates from simple retracking algorithms for airborne radar data may degrade in accuracy over complex topography, due to changes in the return echo shape. Taking this into consideration, the application of the techniques we have described to data from more recent field campaigns, where some in-situ snow depth data have been gathered (e.g. Cavalieri & Markus, 2006), may help shed more light on the questions of radar penetration, and the potential to calculate snow depth from radar and laser altimetry.

Acknowledgments

LaRA was funded by ESA, NASA and the NOAA. Katharine Giles was funded by the National Environmental Research Council. PhD. reference number NER/S/A/2000/03684.

Appendix A

The transmitted power envelope for the D2P is given by

$$P(t) = \mathrm{sinc}^2(\Delta F \pi T) \tag{9}$$

where ΔF is the instrument bandwidth (360×10^6 Hz), and T is given by,

$$T = t - \frac{2r}{c} \tag{10}$$

where r is the range to the surface, t is the time at which the power is being measured and c is the speed of light. r is the distance between the D2P antenna and the facet (Fig. 5), and is given by

$$r = \sqrt{z^2 + (x^2 + y^2)(1 + z^2/Re)} \tag{11}$$

where Re is the earth's radius.

The antenna gain (G) is a function of θ and ϕ, which describe the direction between the antenna boresight and the facet. $G(\theta,\phi)$ is defined as

$$G(\theta,\phi) = \frac{4\pi A_a}{\lambda^2}\left[\frac{1+\cos\theta}{2}\right]^2 \mathrm{sinc}^2\left[\frac{a\pi}{\lambda}\sin\theta\cos\phi\right]\mathrm{sinc}^2\left[\frac{b\pi}{\lambda}\sin\theta\sin\phi\right] \tag{12}$$

where a and b are the lengths of the sides of the antenna. For the D2P a=0.3 m and b=0.15 m. λ is the radar wavelength (0.022 m), and A_a is the area of the antenna (Peebles, 1998).

The D2P uses synthetic aperture processing in the along track direction. The result of the synthetic processing is to narrow the along-track footprint, thereby improving the horizontal resolution of the elevation estimate. The signal to noise ratio of the elevation measurement is improved by multi-looks at each point on the ground from consecutive bursts. Each coherent pulse intersects the antenna gain pattern and the power envelope at a different location, this results in a slightly different shape of power return from each pulse.

To derive the power contribution from the synthetic processing we consider a linear array of N sources. Each source is separated by a distance Δx, given by

$$\Delta x = \frac{v}{\mathrm{prf}} = 0.086m \tag{13}$$

where v is the velocity of the aircraft (150 ms^{-1}) and prf is the pulse repetition frequency (1750 Hz).

The field equation for a linear array of sources is given by, (Peebles, 1998; Stutzman & Thiele, 1998)

$$F_m = \sum_{n=0}^{N-1} e^{\mathrm{i}2n\left(k\Delta x\sin\theta_l - \frac{\pi m}{N}\right)} \tag{14}$$

where $k = \frac{2\pi}{\lambda}$, λ is the wavelength, Δx is the distance between coherent pulses, N is the number of pulses in a coherent burst (16) and m is the pulse number in the burst for which the field equation is being calculated. To calculate the power contribution from each of the 16 pulses, Eq. (14) can be simplified and converted to power as follows (Peebles, 1998; Stutzman & Thiele, 1998).Let

$$\beta = 2\left(k\Delta x\sin\theta_l - \frac{\pi m}{N}\right), \tag{15}$$

therefore

$$F_m = \sum_{n=0}^{N-1} e^{in\beta}. \tag{16}$$

The series is

$$F_m = 1 + e^{i\beta} + e^{i2\beta} + \ldots + e^{i(N-1)\beta}, \tag{17}$$

and multiplying by $e^{i\beta}$ gives

$$F_m e^{i\beta} = e^{i\beta} + e^{i2\beta} + \ldots + e^{iN\beta}. \quad (18)$$

Subtracting Eq. (18) from Eq. (17) gives

$$F_m(1 - e^{i\beta}) = (1 - e^{iN\beta}) \quad (19)$$

$$F_m = \frac{(1 - e^{iN\beta})}{(1 - e^{i\beta})} = \frac{(e^{iN\beta} - 1)}{(e^{i\beta} - 1)} = \frac{e^{iN\beta/2}}{e^{i\beta/2}} \frac{e^{iN\beta/2} - e^{-iN\beta/2}}{e^{i\beta/2} - e^{-i\beta/2}} \quad (20)$$

$$F_m = e^{i(N-1)\beta/2} \frac{\sin(N\beta/2)}{\sin(\beta/2)}. \quad (21)$$

To find the power (P_m) we multiply by the complex conjugate

$$P_m = \frac{\sin^2\left(N\left(k\Delta x \sin\theta_l - \frac{\pi m}{N}\right)\right)}{\sin^2\left(k\Delta x \sin\theta_l - \frac{\pi m}{N}\right)} \quad (22)$$

as

$$e^{i(N-1)\beta/2} e^{i(N-1)\beta/2^*} = 1. \quad (23)$$

The polar response of the facet (P_{res}) is given by

$$P_{\text{res}} = e^{-\left(\frac{\theta_{\text{pr}}}{\varphi_{\text{pr}}}\right)^2} \quad (24)$$

where θ_{pr} is the angle between the vector normal to the facet and the vector between the D2P antenna and the facet and ϕ_{pr} is the polar response angle (Fetterer et al., 1992).

References

Aagaard, K., & Carmack, E. C. (1989, October 15). The role of sea ice and other fresh water in the Arctic circulation. *Journal of Geophysical Research*, *94* (C10), 14,485–14,498.

Beaven, S. G., Lockhart, G. L., Goginei, S. P., Hosseinmostafa, A. R., Jezek, K., Gow, A. J., et al. (1995). Laboratory measurements of radar backscatter from bare and snow-covered saline ice sheets. *International Journal of Remote Sensing*, *16*(5), 851–876.

Bitz, C. M., Holland, M. M., Weaver, A. J., & Eby, M. (2001, February 15). Simulation the ice-thickness distribution in a coupled climate model. *Journal of Geophysical Research*, *106*(C2), 2441–2463.

Cavalieri, D. J., & Markus, T. (2006). *EOS Aqua AMSR-E Arctic sea ice validation program: Arctic 2006 aircraft campaign flight report.* NASA/TM-2006-214142 27 pp.

Comiso, J. C. (2006). Abrupt decline in the Arctic winter sea ice cover. *Geophysical Research Letters*, *33*, L18504. doi:10.1029/2006GL027341

Csathó, B., Thomas, R.H., & Krabill, W.B. (1996). Mapping Ice Sheet Topography with Laser Altimetry in Greenland, BPRC Technical Report No. 96-01, Byrd Polar Research Center, The Ohio State University, Columbus, Ohio, 53 pages.

Curry, J., Schramm, J., & Ebert, E. (1995, Feb). Sea ice-albedo climate feedback mechanism. *Journal of Climate*, *8*(2), 240–247.

ECMWF, (2002)."ECMWF Operationa Analysis data (March 1994–present)", British Atmospheric Data Centre. http://badc.nerc.ac.uk/data/ecmwf-op, 2002.

Ferraro, E. J., & Swift, C. T. (1995, May). Comparison of retracking algorithms using airborne radar and laser altimeter measurements of the Greenland ice sheet. *IEEE Transactions on Geoscience and Remote Sensing*, *33*(3).

Fetterer, F. M., Drinkwater, M. R., Jezek, K. C., Laxon, S. W. C., Onstott, R. G., & Ulander, L. M. H. (1992). Sea ice altimetry. In F. D. Carsey (Ed.), *Microwave Remote Sensing of Sea IceGeophysical monograph*, *Vol. 68*. 1992 Washington D.C. American Geophysical UnionWashington D.C.

Giles, K. A., & Hvidegaard, S. M. (2006, August 10). Comparison of space-borne radar altimetry and airborne laser altimetry over sea ice in the Fram Strait. *International Journal of Remote Sensing*, *27*(15), 3105–3113.

Haas, C. (2002). Validation of CryoSat sea-ice products: Instruments and methods, *Geoscience and Remote Sensing Symposium, 2002. IGARSS '02. 2002 IEEE International*, Volume: 3, pp 1753–1755, 24–28.

Krabill, W., Abdalati, W., Frederick, E., Manizade, S., Martin, C., Sonntag, J., et al. (2002). Aircraft laser altimetry measurement of elevation changes of the Greenland ice sheet: Technique and accuracy assessment. *Journal of Geodynamics*, *34*, 357–376.

Kwok, R., Zwally, H. J., & Yi, D. (2004). ICESat observations of Arctic sea ice: A first look. *Geophysical Research Letters*, *31*, L16401. doi:10.1029/2004GL020309

Laxon, S. W., Peacock, N., & Smith, D. (2003, October 30). High interannual variability of sea ice thickness in the Arctic region. *Nature*, *425*, 947–950. doi:10.1038/nature02050

Ledley, T. S. (1993). Sea Ice: A factor in influencing climate on short and long time scales. In W. R. Peltier (Ed.), *Ice in the climate system*. Berlin: Springer-Verlag.

Leuschen, C., & Raney, R. K. (2005). Initial results of data collected by the APL D2P radar altimeter over land and sea ice. *Johns Hopkins APL Technical Digest*, *26*(2), 114–122.

Mantripp, D. (1996). Radar Altimetry, in The Determination of Geophysical Parameters from Space, Ed. N.E. Fancey, I.D. Gardiner and R.A. Vaughan, Scottish Universities Summer School in Physics and Institute of Physics Publishing, Bristol and Philadelphia.

McLaren, A. S., Barry, R. G., & Bourke, R. H. (1990, June 28). Could Arctic ice be thinning? *Nature*, *345*, 762.

Parashar, S. K., Biggs, A. W., Fung, A. K., & Moore, R. K. (1974, 15-19th April). Investigation of radar discrimination of sea ice. *Proceedings of the 9th International Symp. On Remote Sensing of the Environment, Ann Arbor, MI*, *Vol. 1* (pp. 323–332).

Peacock, N. R., & Laxon, S. W. (2004). Sea surface height determination in the Arctic Ocean from ERS altimetry. *Journal of Geophysical Research*, *109*, C07001. doi:10.1029/2001JC001026

Peebles, P. Z., Jr. (1998). *Radar principles.* New York: John Wiley & Sons, Inc.

Raney, R. K. (1998, September). The Delay/Doppler radar altimeter. *IEEE Transactions on Geoscience and Remote Sensing*, *36*(5).

Raney, R. K., & Leuschen, C. (2003). *Technical support for the deployment of radar and laser altimeters during LaRA 2002.* Johns Hopkins University, Applied Physics Laboratory.

Rothrock, D. A., Zhang, J., & Yu, Y. (2003). The Arctic ice thickness anomaly of the 1990s: A consistent view from observations and models. *Journal of Geophysical Research*, *108*(C3), 3083. doi:10.1029/2001JC001208

Sturm, M., Holmgrem, J., & Perovich, D. K. (2002). Winter snow cover on the sea ice of the Arctic Ocean at the Surface Heat Budget of the Arctic Ocean (SHEBA): Temporal evolution and spatial variability. *Journal of Geophysical Research*, *107*(C10), 8074. doi:10.1029/2000JC000400

Stutzman, W. L., & Thiele, G. A. (1998). *Antenna theory and design.* John Wiley & Sons, Inc.

Wadhams, P., Tucker, W., Krabill, W., Swift, R., Comiso, J., & Davis, N. (1992). Relationship between sea ice freeboard and draft in the Arctic basin, and implications for ice thickness monitoring. *Journal of Geophysical Research*, *97*, 20325–20334.

Warren, S. G., Rigor, I. G., Untersteiner, N., Radionov, V. F., Bryazgin, N. N., Aleksandrov, Y. I., et al. (1999). Snow depth on Arctic sea ice. *Journal of Climate*, *12*(6), 1814–1829.

Wingham, D. J., Forsberg, R., Laxon, S., Lemke, P., Miller, H., Raney, K., et al. (2001, November 14). *CryoSat calibration and validation concept.* Centre for Polar Observation and Modelling : University College London Doc. CS-PL-UCL-SY_004.

Wingham, D., Francis, C. R., Baker, S., Bouzinac, C., Brockley, D., Cullen, R., et al. (2006). CryoSat: A mission to determine the fluctuations in Earth's land and marine ice fields. *Advances in Space Research*, *37*, 841–871.